A Coherent TBD Algorithm for Remote Sensing of Weak Targets Using GNSS Reflected Signals

Ce Zhang, Shuzhu Shi, Jianya Gong, and Rui Li

***Abstract*—Global navigation satellite system (GNSS) reflected signals have been widely used in remote sensing applications. To overcome the low-power budget of GNSS reflected signals, traditional detection strategies involve extending the coherent processing interval (CPI) of a single frame or employing the multiframe detection (MFD) method in which the noncoherent integration is used to accumulate echo energy. In this article, a novel coherent dynamic-programming-based track-before-detect (C-DP-TBD) algorithm is proposed to search and compensate for the interframe phase shift to improve the performance of weak target detection using GNSS reflected signals. The proposed algorithm is included in the two-stage MFD and follows a range-Doppler (RD) map generator. The RD map generator extracts the RD map candidate list for a specific data frame, which contains all of its variants based on the potential phase value and location shifts of the target peak in the RD domain relative to a designated reference frame. Subsequently, the C-DP-TBD processor coherently integrates each variant in this list with the reference frame, removes implausible variants, and selects the most reliable one by comparing all resulting peak signal-to-noise ratios with a preset threshold. The confirmation of the target track in the RD domain is finally achieved by extracting the position of the target peak from every available frame. Compared with traditional motion target detection methods with long CPI and DP-TBD methods, the performance superiority of the proposed algorithm is demonstrated by both simulation and experimental results in which a ferry was employed as a moving target.**

***Index Terms*—Dynamic-programming-based track-before-detect (DP-TBD), global navigation satellite system (GNSS), interframe coherent integration, multiframe detection (MFD), passive remote sensing, weak target detection.**

I. Introduction

THE concept of utilizing global positioning system (GPS) signals reflected from the Earth's surface for scatterometry was initially proposed in 1988 [1]. Since the launch of the first GPS satellite in 1989, researchers have continuously explored the potential applications of global navigation satellite system (GNSS) reflected signals in various environment remote sensing fields, including the GNSS-reflectometry (GNSS-R) technique used for Earth observation, such as wind speed retrieval [2], [3], sea surface height measurement [4], [5], soil moisture estimation [6], [7], and the space-surface bistatic synthetic aperture radar technique used for coherent change detection [8]. Besides these applications, moving target detection (MTD) is also a task of interest for GNSS-based remote sensing systems. Different from the moving target indication technique employed in remote sensing imagery [9], [10], the task of MTD for GNSS-based passive remote sensing systems is often achieved in the azimuth-frequency domain, such as the delay-Doppler map processing in GNSS-R technique [11], [12], [13], [14] and the range-Doppler (RD) map processing in GNSS-based passive radar technique [15], [16], [17].

Nevertheless, the low power of the GNSS scattered signal limits the detection performance of GNSS remote sensing systems, particularly for those reflected from maneuvering targets. Since the coherent processing interval (CPI) of a single frame cannot be infinitely extended, to enhance the performance of the GNSS-based passive radar system, it becomes necessary to exploit methodologies for detecting the weak target by fusing multiple frames of data. Whether the fusion procedure involves frames from one or multiple satellites, this process aligns with the concept of a multiframe detection (MFD) problem, and track-before-detect (TBD) has been proven to be an effective approach for handling such problems [18]. The fundamental operation of TBD is to accumulate echo energy along a potential trajectory before formally asserting the presence of the target, often with a sufficiently low threshold or even with no threshold. The basic TBD strategy operates as a brute-force traversal algorithm in which all conceivable cases are examined. However, when echo data are divided into multiple frames, the potential number of tracks of a moving target becomes enormous. Implementing TBD directly under such circumstances is nearly impossible due to the exponential increase in algorithmic complexity with the growing number of frames. Fortunately, several advanced iterations of TBD have been developed to enhance its practicality, and dynamic-programming TBD (DP-TBD) is one of the most commonly used methods [19], [20]. It divides the whole frame chain into several shorter segments and generates the corresponding target track. This approach effectively reduces the computational complexity of the problem from exponential to linear if the solution can be obtained for each segment.

Traditional DP-TBD is specifically developed to process echo data obtained by actively scanned radar with noncoherent integration that contributes to the signal-to-noise ratio (SNR) enhancement of echo pulses in the time domain, but the obtained gain is reduced for energy focusing in the RD domain. Thus,

Manuscript received 29 January 2024; revised 18 March 2024 and 28 April 2024; accepted 5 June 2024. Date of publication 10 June 2024; date of current version 18 June 2024. *(Corresponding author: Shuzhu Shi.)*

Ce Zhang, Shuzhu Shi, and Jianya Gong are with the School of Remote Sensing and Information Engineering, Wuhan University, Wuhan 430079, China (e-mail: zhangce@whu.edu.cn; shuzhushi@hotmail.com; gongjy@whu.edu.cn).

Rui Li is with the Beijing Institute of Remote Sensing Information, Beijing 100192, China. (e-mail: 1103389026@qq.com).

Digital Object Identifier 10.1109/JSTARS.2024.3411876

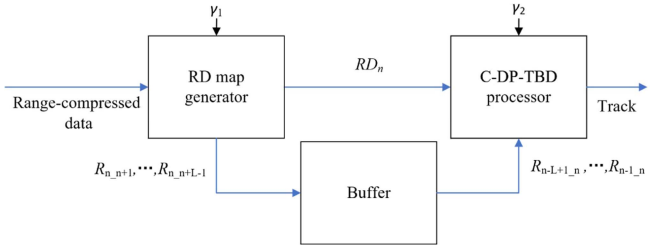

Fig. 1. Block diagram of the two-stage target detection method.

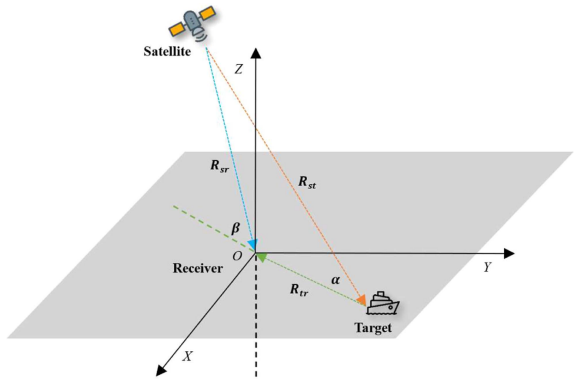

Fig. 2. Geometric configuration of our radar system.

although DP-TBD can be well applied to MFD strategies for the GNSS-based passive radar system, its performance is deteriorated by the noncoherent integration [21], [22]. In contrast, coherent integration is usually considered to be one of the useful methods to effectively detect a weak target. Some work has been conducted to improve the MFD technique with coherent integration, but most of them were validated by simulation or experimental results in which stationary targets were employed [23], [24], [25]. In the practical detection of moving targets, coherent integration is challenging due to the unpredictable and unstable interframe phase shift among echo signals produced by different satellites, even for those produced by the same illuminating satellite but received at different times. Under these conditions, to detect a target merged by severe noise, traditional DP-TBD algorithms should be improved to incorporate the capability to compensate for the interframe phase shifts. This improved strategy is referred to as coherent DP-TBD (C-DP-TBD) in this article.

The proposed weak target detection method mainly consists of two processors, i.e., the RD map generator with a threshold γ_1 and the C-DP-TBD processor that has a threshold γ_2 and a segment size of L. The block diagram of the detection method is shown in Fig. 1.

In Fig. 1, RD_n represents the nth RD map. R stands for RD map candidate list and the subscript indicates the index of the current frame along with the reference frame, separated by an underscore. This method takes the range-compressed data stream as its input and outputs the target's motion track in the RD domain. In the RD map generator, the 1-D continuous signals are segmented into a 2-D data array, and then range cell migration (RCM) and Doppler cell migration (DCM) are corrected using the keystone transform (KT) and dechirp algorithm (DA), respectively, ensuring intraframe signal coherence. However, owing to the low SNR of the echo signals, it is challenging to distinguish the echo peak in the RD domain. The target peak buried by background noise may be located in various positions and can have diverse phase values, resulting in different compensation parameters used to maintain the interframe signal coherence. After the reference frame is produced, each frame involved in the current segment is processed to produce a candidate list of RD maps. This list contains all possible RD maps according to every compensation parameter that can meet the constraints for both interframe phase shift and motion parameter, i.e., the location and phase of the target peak. This list is then transferred to the C-DP-TBD processor, where it generates all potential target tracks within frames in the same segment. Following the operations of track pruning and confirmation, the C-DP-TBD processor removes improbable results and retains the most plausible set of target peak information. Simultaneously, the buffer, along with the most recent segment of the target track, undergoes updating.

To validate the effectiveness of the proposed algorithm, both simulation and practical experiments were conducted in which a ferry was adopted as the moving target. The experimental results were then compared with the automatic identification system (AIS) data characterizing the real motion of the target. The outcomes verified the tracking and detection capabilities of our algorithm, even when the target cannot be visible in the raw RD map.

The rest of this article is organized as follows. Section II introduces the signal model and the RD map generation. Section III describes the processing strategy of the C-DP-TBD algorithm. The simulation and experimental results are provided in Section IV and Section V, respectively. Finally, Section VI concludes this article.

II. Signal Model and RD Map Generation

In this section, we briefly recall the signal model and RD map generation of the GNSS-based passive radar system. A more detailed description can be found in our previous work [26].

GNSS-based passive radar systems always adopt a bistatic configuration. In our study, satellites from the BeiDou navigation satellite system (BDS) were employed as transmitters. The geometric configuration of our bistatic radar system is shown in Fig. 2. Here, a ferry is chosen as the target to be detected. Furthermore, R_{st} represents the range between the satellite and the target, R_{tr} is the range between the target and the receiver, and R_{sr} is the range between the satellite and the receiver. The bistatic angle is denoted as α and the angle between the receiver-to-target and receiver-to-satellite orientations is defined by β. Furthermore, R_{delta} represents the bistatic range. Due to the bistatic configuration, R_{delta} no longer equals $2R_{\mathrm{tr}}$ in the case of monostatic radar setup. As a result, the relationship between them is represented with a coefficient k, i.e., $R_{\mathrm{delta}} = kR_{\mathrm{tr}}$. Moreover, k can be calculated by

$$k = \frac{\sin(\beta) - \sin(\alpha)}{\sin(\beta)\cos(\alpha) - \cos(\beta)\sin(\alpha)} + 1. \tag{1}$$

Coefficient k is usually positive, and its specific value depends on the bistatic configuration. For a monostatic radar system, the value of k can be calculated to be 2 in terms of (1).

The range-compressed signal, which is acquired through a cross correlation between the received echo signal and the reference signal reconstructed with the direct signal, can be expressed as follows:

$$s(t) = A\rho\left(t - \frac{kR_{\text{tr}}}{c}\right)\exp\left(-j2\pi f_0\frac{kR_{\text{tr}}}{c}\right) \tag{2}$$

where A is the signal amplitude, ρ is the envelope in the range-time dimension, f_0 stands for the carrier frequency, and c is the speed of light.

The anticipated targets in our study are maritime objects, such as vessels or ferries. Due to the relatively simple motion parameters of these targets, their motion can often be expressed as a second-order polynomial within a short CPI, i.e., a few seconds. In this case, the target undergoes translational motion with a constant acceleration within one frame, and high-order movement parameters, such as jolt or rotational angular velocity, need not be considered any longer. Therefore, using the second-order Tylor series R_{tr} can be expressed with the radial acceleration a, the radial velocity v, and the initial target distance R_0, and can be written as follows:

$$R_{\text{tr}} \approx R_0 + vt + \frac{1}{2}at^2. \tag{3}$$

The signals transmitted by GNSS satellites are continuous waves and need to be organized into a 2-D array using a specific pulse repetition frequency (PRF). Since the PRF of the BDS B3I signal is 1 kHz, the range-compressed signal, as represented by (2), can be segmented into a 2-D form as follows:

$$s(\tau, t_m) = A\rho\left(\tau - \frac{2kR_0 + 2kvt_m + kat_m^2}{2c}\right) \times \exp\left(-j2\pi f_0\frac{2kR_0 + 2kvt_m + kat_m^2}{2c}\right) \tag{4}$$

where τ and t_m represent the fast-time and slow-time variables, respectively.

It is noteworthy to mention that the envelope of the received signal in the azimuth-time dimension, which is associated with the radiation pattern of the receiving antenna, is neglected in our study. Moreover, the mathematical expression of the complex range-compressed signal obtained from a single GNSS satellite is given by (4). When different GNSS satellites are used for target detection, the specific values of amplitude A, envelope ρ, and coefficient k should be adjusted. However, since the motion parameters adopted in (4) are all radial parameters, the values of amplitude A, envelope ρ, and coefficient k remain constant for the same target and illuminator when a short CPI is adopted.

With an appropriate selection of single-frame CPI, range-compressed data can be transformed into the RD domain for further detection through three main steps, i.e., RCM correction, DCM correction, and discrete Fourier transform (DFT) in the azimuth direction, as shown in the block of "RD map generator" in Fig. 2.

KT is a classic range cell walk correction algorithm that does not require prior knowledge of radial velocity. It involves a rescaling process in the azimuth-time domain, and thus, we introduce the parameter $\hat{t}_m$ to represent the new azimuth-time axis as follows:

$$t_m = \frac{f_0}{f_0 + f_r}\hat{t}_m = \frac{1}{1+\alpha}\hat{t}_m. \tag{5}$$

In our study, the RCM correction was implemented with KT in the range-frequency and azimuth-time domain because the range walk in the envelope can be converted into the phase term by DFT in the range direction. The processed result is given by

$$S_{FT}(f_r, t_m) = AP(f_r)\exp\left[-j2\pi(f_0 + f_r)\frac{kR_0}{c}\right] \times \exp\left[j2\pi(1+\alpha)f_{d0}t_m\right]\exp\left(j\pi\gamma_a {t_m}^2\right) \tag{6}$$

where $f_{d0} = -kv/\lambda$, $\gamma_a = -ka/\lambda$, $\alpha = f_r/f_0$, f_r denotes the frequency in the range direction, and $P(f_r)$ is the new envelope in the range-frequency domain.

Then, the old azimuth-time variable t_m should be replaced with the new term $\hat{t}_m$, and the signal can be rewritten as follows:

$$S_{FA}(f_r, \hat{t}_m) = AP(f_r)\exp\left[-j2\pi(f_0 + f_r)\frac{kR_0}{c}\right] \times \exp\left(j2\pi f_{d0}\hat{t}_m\right)\exp\left[j\frac{\pi\gamma_a}{(1+\alpha)^2}\hat{t}_m^2\right]. \tag{7}$$

For the BDS B3I signal, the relationship $f_r \ll f_0$ always holds, and hence, we get $1 + \alpha \approx 1$. Based on this approximation, (7) can be rewritten as follows:

$$S_{FA}(f_r, \hat{t}_m) = AP(f_r)\exp\left[-j2\pi(f_0 + f_r)\frac{kR_0}{c}\right] \times \exp\left(j2\pi f_{d0}\hat{t}_m\right)\exp\left(j\pi\gamma_a\hat{t}_m^2\right). \tag{8}$$

Subsequently, the signal needs to be transformed back to the range-time domain through an inverse DFT, and the new time-domain signal can be written as

$$s(\tau, \hat{t}_m) = A\rho\left(\tau - \frac{kR_0}{c}\right)\exp\left(-j\frac{2\pi f_0 kR_0}{c}\right) \times \exp\left(j2\pi f_{d0}\hat{t}_m\right)\exp\left(j\pi\gamma_a\hat{t}_m^2\right). \tag{9}$$

After RCM is corrected by KT, we employ the DA to perform DCM correction. DA involves a search for the Doppler rate, which is related to the radial acceleration along the range bin corresponding to kR_0/c. With the determined Doppler rate, the second-order phase shift associated with the last term in (9) can be compensated directly to complete the DCM correction. If the SNR after KT is adequate for the implementation of DA, the result without a constant phase term can be expressed by

$$s(\tau, \hat{t}_m) = A\rho\left(\tau - \frac{kR_0}{c}\right)\exp\left(j2\pi f_{d0}\hat{t}_m\right). \tag{10}$$

It can be found that the signal in the azimuth-time domain after an ideal DCM compensation has a single-frequency form.

Consequently, the energy of the frame can be concentrated in the azimuth-frequency domain, or the RD domain, as described by

$$S_{\mathrm{RD}}(\tau, f_a) = A\rho\left(\tau - \frac{kR_0}{c}\right)\mathrm{sinc}\left[T\left(f_a - f_{d0}\right)\right]. \quad (11)$$

It is worth mentioning here that only maps in which the target peak exceeds the SNR threshold γ_1 are considered to be valid RD maps. Furthermore, to accurately represent each valid frame within the entire captured intermediate frequency data, we rewrite the signal in the *n*th RD map as $\mathrm{RD}_n(\tau, f_a)$

$$\mathrm{RD}_n(\tau, f_a) = A_n\rho\left(\tau - \frac{kR_{0\_n}}{c}\right)\mathrm{sinc}\left[T\left(f_a - f_{d0\_n}\right)\right] \times \exp\left(j\varphi_{0\_n}\right) + N_n \quad (12)$$

where R_{0_n} stands for the target's initial location in the *n*th frame, and f_{d0_n} is the corresponding Doppler shift. To represent the difference among frames, two parameters are introduced: φ_{0_n} is the initial phase of the *n*th frame and can also be regarded as the phase of the target peak in the RD domain, and N_n is the 2-D background noise contained in the *n*th RD map.

Finally, let us introduce a technique to choose the proper starting point of the sampled signal, which is referred to as level alignment (LA). This operation is necessary for both the GNSS signal acquisition stage and the RD map generation stage. However, it has been rarely discussed in similar previous works. The start of data sampling in the receiver can occur at any time within the period of ranging code. Furthermore, due to the presence of at least one higher level code, such as the data code modulated on the ranging code, this phenomenon can introduce potential phase inversion during one sample. Taking the BDS B3I signal as an example, if the start of data sampling is precisely located in the middle of the period, and the two nearest adjacent data levels are inversed, the cross-correlation value of the samples with the local ranging code in the first millisecond would equal to zero. The actual situation might not be as bad as that described above but always brings out the energy loss after range compression. Although this problem is usually solved automatically in the tracking stage of the GNSS receiver, our passive radar system operates in parallel processing mode in which the receiver processes the direct and reflected signals simultaneously. In our study, the LA technique was adopted to address this problem. LA was implemented by pushing the start of data sampling to the location indicated by the code phase that was given by the initial GNSS signal acquisition step. With the LA technique, the start of the sampled data can be realigned with the beginning of one period of the ranging code. Obviously, LA is significant for eliminating the energy loss during accumulation, which is caused by different data levels within a CPI.

III. Weak Target Detection Algorithm

In this section, coherent and noncoherent integrations adopted for MFD are first introduced briefly. Next, the selection of the CPI is described. Finally, the proposed C-DP-TBD algorithm is introduced.

A flowchart of the MFD procedure, including the C-DP-TBD algorithm, is shown in Fig. 3. Compared with Fig. 1, Fig. 3 offers a more detailed description of the data processing methodology adopted in the weak target detection solution. Specifically, through considering the interframe phase shift and its corresponding kinematic parameters based on the prior knowledge of target motion, constraints for the parameter change of interframe target peak are first imposed, and then the RD map generator produces the candidate list of RD maps according to every compensation parameter that can meet the imposed constraints. Subsequently, the generated candidate list is transferred to the C-DP-TBD processor, which mainly consists of three modules, i.e., the track generation module, the track pruning module, and the track confirmation module. In practical operation, the track generation module enumerates and stores all plausible target tracks based on the input candidate list of RD maps. The track pruning module selects the track with the highest coherently accumulative energy. Finally, the reliability of the extracted target track is ascertained by the track confirmation module according to the threshold γ_2. These modules will be further discussed in the following sections. In addition, these operations highlighted by brackets in Fig. 3 are distinctive features of the proposed C-DP-TBD algorithm compared with the traditional DP-TBD algorithms.

A. Coherent and Noncoherent Integrations Adopted for MFD

If the number of integrated pulses is denoted as Num, an increase in the signal power by a factor of Num^2 can be achieved by both noncoherent and coherent integrations when the interpulse phase shift is not considered. Regarding the ideal white Gaussian noise, its power increased by a factor of Num can be achieved by coherent integration, given that the noise samples are independent and zero mean. However, it is difficult to determine the increased factor of noise power in the case of noncoherent integration because the cross products of signal and noise components are usually generated by nonlinear transformations. Nevertheless, the noncoherent integration of pulses in the time domain can still improve the SNR because the increased factor of the noise power in the case of noncoherent integration was proven to be smaller than that of the signal power [27], [28]. However, this conclusion no longer holds for the noncoherent integration of RD maps. This is not only because the background noise no longer conforms to an ideal power distribution after range compression and a DFT along the azimuth time but also because the colored noise in practice has different inherent characteristics from the ideal white noise. In addition, experimental results are provided here to illustrate how the average noise amplitude varies with the number of frames when the coherent and noncoherent integrations are employed individually. The BDS geostationary Earth orbit (GEO) 04 satellite was adopted as the transmitter of opportunity to detect a stationary target in this experiment, and a total of 80 frames with a CPI of 1 s were achieved. Fig. 4 shows the variance of the average noise amplitude in the case of coherent or noncoherent integration of data frames.

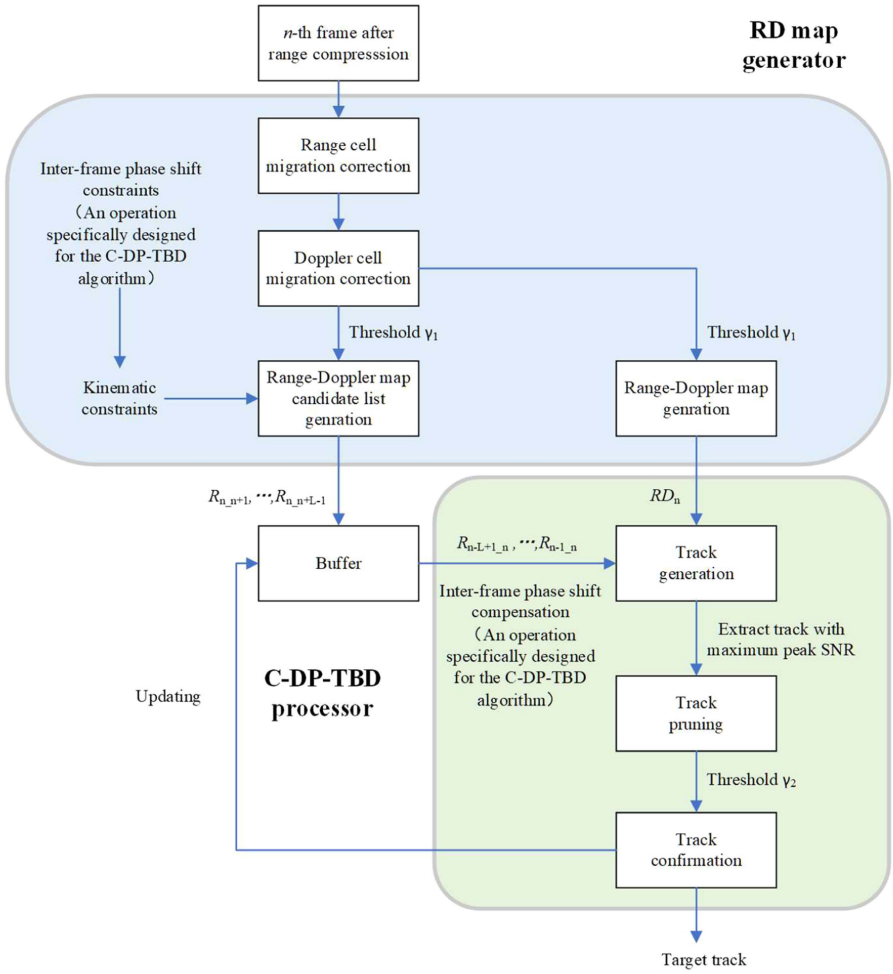

Fig. 3. Flowchart of the MFD procedure, including the proposed C-DP-TBD algorithm.

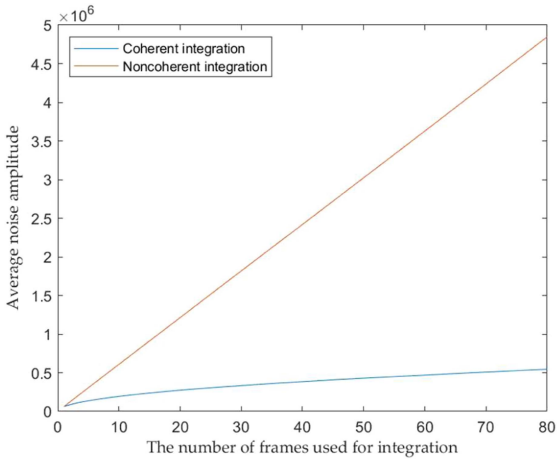

Fig. 4. Variance of the average noise amplitude in the case of coherent or incoherent integration of data frames.

It can be found that both integration methods can improve the average noise amplitude. However, Fig. 4 shows that the rate of change is about Num for noncoherent integration and about $\sqrt{\text{Num}}$ for coherent integration. Therefore, a lower background noise power can be achieved by the coherent integration of echo signals compared with the noncoherent integration method. Nevertheless, the practical implementation of coherent integration is challenging because it is difficult to calculate the phase value of the target peak in the RD domain. Although some theoretical functions can be introduced to express the phase term, the actual phase variation of the target peak is entirely chaotic in practical cases. We took a stationary target having the strongest echo power in our experiment as an example, and the phase variation of its echo peak for each frame is shown in Fig. 5. It can be observed that it is difficult to use a mathematical formula to express the phase variation of the target peak for each frame, even for a stationary target. Not only the motion parameters, which cannot be accurately expressed by the motion polynomial, but also the background noise and various interferences can significantly impact the phase of the target peak. If such phase values are maintained during the coherent integration, the amplitude of the target peak will unavoidably suffer from deterioration. Based on the above analysis, it can be found that coherent integration is more advantageous for MFD than noncoherent integration only if the interframe coherence shift can be well corrected. As a result, the C-DP-TBD algorithm is proposed to perform the coherent integration for MFD.

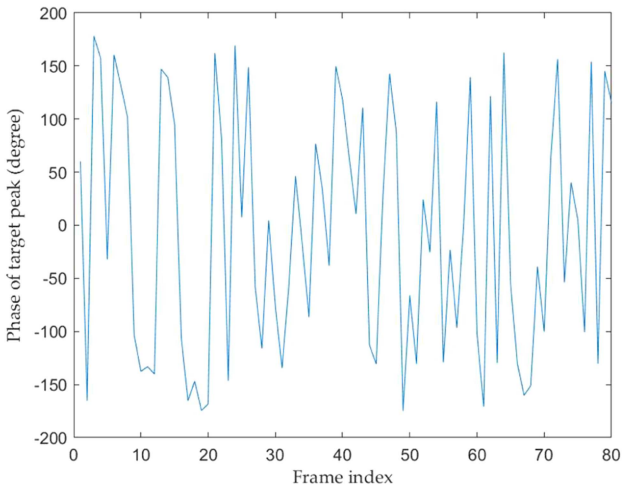

Fig. 5. Phase variation of a stationary target's echo peak for each frame.

B. Selection of CPI

In the traditional MTD tasks, CPI is defined as the time length of a single frame. While in MFD, it represents the cumulative dwell time of multiple frames. To distinguish the difference in CPI in these two cases, we introduce a new parameter referred to as the coherent integration length (CIL) in the following discussion, which is used to represent the number of frames adopted in MFD methods.

The CPI is undoubtedly one of the most crucial parameters in the whole target detection procedure. However, the selection of CPI has been rarely discussed, and its specific value is usually determined in terms of empirical value or by comparing the obtained SNR values under the condition of different CPIs to find the appropriate value [15]. The determination of the minimum CPI required for target detection is mainly influenced by the detection threshold and is difficult to implement in practice because the practical noise power is hard to accurately model. This difficulty is particularly pronounced for noncoherent integration in the RD domain, where traditional threshold-setting methods, such as Albersheim's detection formula, cannot be directly applied [27]. Consequently, practical target detection tasks often resort to adaptive threshold-setting strategies, such as the constant false alarm rate (FAR) detection [29], [30]. To simplify this problem, we set the minimum required SNR directly equal to the threshold γ_2. In other words, a peak exceeding this SNR threshold indicates the presence of a target in the RD domain.

Since the coherent integration was adopted for MFD in our work, the rate at which the SNR changes with the number of frames used for integration can be calculated as $\sqrt{\text{Num}}$ in linear scale, as discussed in Section III-A. If the SNR of a frame with a CPI of 1 s is denoted by $\text{SNR}_{\text{input}}$ in linear scale, the relationship between the minimum required integration time CPI_{min} in seconds and the value of γ_2 in linear scale can be expressed by

$$\text{CPI}_{\text{min}} = \left(\frac{\gamma_2}{\text{SNR}_{\text{input}}} \right)^2. \tag{13}$$

When multiple frames with a CPI of 1 s are adopted for MFD, the minimum CIL can be calculated by

$$\text{CIL}_{\text{min}} = I\left(\text{CPI}_{\text{min}}/1\right) \tag{14}$$

where I stands for the rounding-up operation. For frames whose CPI is not 1 s, CIL_{min} can be calculated by replacing the denominator with the specific value of CPI.

To ensure the performance of DFT, the residual range walk after RCM correction should be within the size of one range cell, which is equal to c/kf_s. Here, f_s is the sampling rate of the intermediate frequency signal. Thus, after proper first-order RCM correction, according to (3), the maximum CPI can be written as

$$\text{CPI}_{\text{max}} = \sqrt{2c/kf_s a_{\text{max}}} \tag{15}$$

where a_{max} represents the maximum radial acceleration. It is worth noting that CPI_{max} only serves as a constraint for single-frame processing. For the MFD, CPI_{max} applies to the generation process of each input RD map.

The above discussions demonstrate that the limit of CPI can be theoretically determined in terms of the preset SNR threshold and the predicted target motion parameters, but in practice, the upper bound of CPI given by (15) often needs to be reduced mainly due to two factors. First, even with proper RCM and DCM corrections, the power of the echo signal scattered by the detected target tends to spread across multiple RD cells. This phenomenon is known as the target scintillation mainly produced by the shift of the effective reflection points on the target. A shorter CPI is usually required to mitigate the impact of target scintillation in the RD domain. Second, the phase shift introduced by the Doppler rate can be adequately compensated with a successful DCM correction. However, in the case of low SNR, the DCM correction might not work effectively because the search for the Doppler rate often relies on a discernible trajectory of the range-compressed peak in the range-time domain, and this might not be achievable in this case. The potential failure of DCM correction also necessitates a shorter CPI to maintain intraframe phase coherence.

In practice, CPI_{max} is sometimes smaller than CPI_{min}. This indicates that the weak target detection problem cannot be effectively addressed with the single-frame MTD, and the MFD method should be employed instead. Further discussions about this topic will be provided in Sections IV and V.

C. C-DP-TBD Algorithm

Different from the traditional TBD algorithms, the DP-TBD algorithm divides the entire frame chain into smaller segments and solves the detection problem within each segment iteratively. The most important prerequisite for this solution is that the detection problem within each segment can be solved individually, and then, the computational complexity of the tracking task could be reduced significantly. We define the smallest size of a segment as L, which can be calculated by (14) and the total number of available frames as R. Furthermore, the period of data used to produce each input RD map is denoted as T_C.

Initial and normal detections are the two main steps in our proposed algorithm. To better illustrate the target detection procedure, we assume that no target peak can be visible in all frames. Therefore, the initial detection, which involves the first L frames, has the maximum computational load. Fortunately, it can be decreased by imposing constraints on the motion parameters of the detected target. Specifically, the range of radial velocity and acceleration can be expressed as $v_{\min} \le v \le v_{\max}$ and $a_{\min} \le a \le a_{\max}$, respectively. Subsequently, the range walk R_{walk} between two frames should be within the range described by

$$\frac{1}{2}a_{\min}{T_C}^2 + v_{\min}T_C \le R_{\text{walk}} \le \frac{1}{2}a_{\max}{T_C}^2 + v_{\max}T_C. \quad (16)$$

The number of corresponding range cell M can be calculated as

$$M = I\left(\left[\frac{1}{2}\left(a_{\max} - a_{\min}\right){T_C}^2 + \left(v_{\max} - v_{\min}\right)T_C\right]\frac{kf_s}{c}\right). \quad (17)$$

Similarly, the size of an azimuth-frequency cell, which also corresponds to the frequency resolution, is $/l_a$, where l_a is the number of points along the azimuth direction of one frame. Consequently, the range of Doppler shift walk fd_{walk} between two frames can be described by

$$-2a_{\max}T_C/\lambda \le f_{\text{walk}} \le -2a_{\min}T_C/\lambda \quad (18)$$

where λ is the wavelength of the transmitted signal.

As a result, the number of azimuth-frequency cell P can be calculated as

$$P = I\left(\frac{2\left(a_{\max} - a_{\min}\right)T_C l_a}{\lambda \text{PRF}}\right). \quad (19)$$

Because the phase term of the target peak in the RD map cannot be predicted, a step is needed to search for its value. Due to its randomization, each angle in the complex plane is possible. Therefore, the searching number Q of the phase term is only dependent on the searching step σ in degrees and can be expressed as

$$Q = I\left(360/\sigma\right) \quad (20)$$

where the number 360 represents the search range of phase in degrees. Note that the phase value under consideration in this work is confined to the wrapped one.

To compensate for the first RD map RD_1 to have the same peak location in the RD domain and the same phase of this target peak as those in the nth RD map RD_n, the number of the possibilities $\text{PO}_{n,1}$ can be defined as

$$\text{PO}_{n,1} = (n-1)^2 \times M \times P \times Q. \quad (21)$$

For the initial detection with the first L frames, the total number of possibilities to generate the Lth RD map RD_L or the number of possible target tracks ended with the Lth frame can be defined as

$$\text{PO}_L = \prod_{u=1}^{L-1} u^2 \times M \times P \times Q. \quad (22)$$

The multiplier u is introduced based on the fact that the larger the time difference among these frames, the longer the range of both range and velocity walks. Equation (22) indicates that the number of possible target tracks would be enormous if L is large. Because none of these possibilities can be replicated with each other, PO_L cannot be reduced as long as the target is invisible in these L frames by any means. Fortunately, this complex detection process only needs to be executed once. In each step of the subsequent normal detections, since all target motion parameters are known except for the last frame, the total number of possible target tracks ended with the Rth frame can be expressed as

$$\text{PO}_{\text{all}} = (R-L) \times M \times P \times Q + \prod_{u=1}^{L-1} u^2 \times M \times P \times Q. \quad (23)$$

From (23), it can be found that the number of possible target tracks in normal detection is reduced dramatically to $M \times P \times Q$. Note that (23) only holds when the target can be tracked and detected in the RD domain for all frames through initial and normal detections. Through taking a look back at the initial detection, we set the Lth frame RD_L to be the reference, and RD_L can be represented by RD_u as $\text{RD}_{L,u}$ according to the signal expression given by (12)

$$\begin{aligned}\text{RD}_{L,u}(\tau, f_a) = A_u \rho\left(\tau - \frac{k\left(R_{0\_u} + R_{w,L,u}\right)}{c}\right) \\ \times \text{sinc}\left[T\left(f_a - \left(f_{d0\_u} + f_{w,L,u}\right)\right)\right] \\ \times \exp\left(j\varphi_{0\_u} + j\varphi_{w,L,u}\right) + N_u\end{aligned} \quad (24)$$

where $R_{w,L,u}$, $f_{w,L,u}$, and $\varphi_{w,L,u}$ are the possible range walk, frequency walk, and phase shift between the uth and Lth frames, respectively. All these possibilities can be determined according to the kinematic constraints described by (16) and (18), and (24) illustrates one possibility in the candidate list R_u. Note that $\text{RD}_{L,u}$ is different from RD_L, mainly because of the different noise powers and amplitudes of the target peak shown in these two maps. In addition, although the target is buried by noise in RD_L, the correct target detection result can still be obtained with $\text{RD}_{L,u}$. It is worth mentioning here that only maps in which the peak SNR exceeds the threshold γ_1 can be confirmed as eligible ones and are further processed in the manner described by (24). In practical operation, since the target may be invisible in the RD domain, we set γ_1 to $-\infty$ to preserve as much signal energy as possible. With this operation, both the probability of detection and FAR are increased, but the FAR can be reduced in the subsequent track confirmation operation with a higher threshold γ_2. This reduction is attributed to the SNR enhancement achieved by the coherent integration.

For each of the first $L-1$ frames, the operation expressed by (24) is implemented to align the location and phase value of its target peak with those of the Lth frame. Each case in the PO_L possibilities will generate a distinct RD map, along with a unique target track. This operation is represented as the track generation module in Fig. 3. Furthermore, each case in the PO_L possibilities is a 2-D array whose size is $(L-1)$ by three. We define this

array as $\Theta_{L,s}(R_u, f_u, \varphi_u)$, which contains the range walk, frequency walk, and interframe phase shift between the *u*th and the *L*th frame. Here, $u \in \{1, 2, \ldots, L-1\}$, $s \in \{1, 2, \ldots, \mathrm{PO}_L\}$. Moreover, we define the operation used to select the RD map having the maximum peak SNR as Υ. Note that Υ also represents the pruning operation in Fig. 3, which is used to select the most reliable track from all possible ones. Therefore, for the first $L-1$ frames, the array E_L, which represents the results of initial detection, can be described by

$$E_L(R_u, f_u, \varphi_u) = \underset{s\in\{1,2,\ldots,\mathrm{PO}_L\}}{\operatorname{argmax}} \Upsilon\left(\sum_{u=1}^{L-1} \mathrm{RD}_{L,u,s} + \mathrm{RD}_L\right) \tag{25}$$

where $\mathrm{RD}_{L,u,s}$ stands for the *L*th frame represented by the *u*th frame with the parameter array $\Theta_{L,s}$.

For the *L*th frame, the range cell index R_L, the Doppler shift f_L, and the phase φ_L of the target peak can also be extracted from the operation described by (25). Moreover, the array F_L used to represent the detection result for the *L*th frame can be described by

$$F_L(R_L, f_L, \varphi_L) = \underset{s\in\{1,2,\ldots,\mathrm{PO}_L\}}{\operatorname{argmax}} \Upsilon\left(\sum_{u=1}^{L-1} \mathrm{RD}_{L,u,s} + \mathrm{RD}_L\right). \tag{26}$$

The value of the peak SNR in the initial detection result can be expressed as

$$G_L = \max_{s\in\{1,2,\ldots,\mathrm{PO}_L\}} \Upsilon\left(\sum_{u=1}^{L-1} \mathrm{RD}_{L,u,s} + \mathrm{RD}_L\right). \tag{27}$$

In the track confirmation module, as illustrated in Fig. 3, the processor confirms the current iteration as a valid detection only when the extracted peak SNR, denoted as G_L, surpasses the predetermined threshold γ_2. If a valid detection cannot be achieved with the initial L frames, the processor shifts the starting index of L frames used for the initial detection backward in sequence until the target is detected. Successful detection and tracking of the target within these L input frames are achieved after accurately extracting the peak locations in the RD domain, as demonstrated by (25) and (26).

Compared with the initial detection, the subsequent normal detection would be much easier because only the reference frame has unknown target information. For detection with frames whose index is $n+L-1$, those frames whose index ranges from n to $n+L-2$ need to be integrated in the first place to form a new RD map. Here, the range of n is denoted as $1 < n \le R-L+1$. The signal in the resulting map can be described by

$$\mathrm{RD}_{n+L-2,\mathrm{new}}(\tau, f_a) = \sum_{u=n}^{n+L-2} \left\{ A_u \rho\left(\tau - \frac{kR_{n+L-2\_\mathrm{res}}}{c}\right) \times \mathrm{sinc}\left[T\left(f_a - f_{n+L-2\_\mathrm{res}}\right)\right] \exp\left(j\varphi_{n+L-2\_\mathrm{res}}\right) + N_u \right\} \tag{28}$$

where the subscript res is used to represent the confirmed range cell index, frequency cell index, and phase term of that specific frame by $R_{u\_\mathrm{res}} = R_L - R_u$, $f_{u\_\mathrm{res}} = f_L - f_u$, and $\varphi_{u\_\mathrm{res}} = \varphi_L - \varphi_u$, respectively.

The detection result for the frame whose index is $n+L-1$ can be described by

$$F_{n+L-1}(R_{n+L-1}, f_{n+L-1}, \varphi_{n+L-1}) = \underset{s\in\{1,2,\ldots,\mathrm{PO}_{n+L-1}\}}{\operatorname{argmax}} \Upsilon\left(\mathrm{RD}_{n+L-2,\mathrm{new}} + \mathrm{RD}_{n+L-1}\right). \tag{29}$$

At the same time, the maximum SNR of the echo signal in the frame whose index is $n+L-1$ can be written as

$$G_{n+L-1} = \max_{s\in\{1,2,\ldots,\mathrm{PO}_{n+L-1}\}} \Upsilon\left(\mathrm{RD}_{n+L-2,\mathrm{new}} + \mathrm{RD}_{n+L-1}\right). \tag{30}$$

Similar to the initial detection, only iterations in which the peak SNR exceeds γ_2 are confirmed as valid detections in normal detection, and their corresponding target tracks are extracted. If no target is detected within these frames, the processor will mark this iteration as one track loss and then shift the starting index of L frames used for the normal detection backward in sequence until the target is detected. Note that adjusting the starting index of L frames used for the normal detection would increase the computational complexity of the algorithm. This is attributed to the introduction of frames containing unknown target information, and the extent of this increase is dependent upon the number of track losses. In the C-DP-TBD processor, the track loss is allowed and its number is constrained by an upper bound represented by max_miss. If the total number of track losses exceeds the upper bound, the processor will determine that the algorithm has failed.

In terms of the final processed results of the proposed algorithm, the signals within SNR-enhanced RD maps whose indices are $u \in \{1, 2, \ldots, L-1\}$ can be written as

$$\mathrm{RD}_{u\_\mathrm{res}}(\tau, f_a) = A_{L\_\mathrm{res}} \rho\left(\tau - \frac{kR_{u\_\mathrm{res}}}{c}\right) \times \mathrm{sinc}\left[T\left(f_a - f_{u\_\mathrm{res}}\right)\right] * \exp\left(j\varphi_{u\_\mathrm{res}}\right) + N_{L\_\mathrm{res}} \tag{31}$$

where A_{L_res} and N_{L_res} represent the echo amplitude and background noise after the initial detection for the *L*th frame, respectively. These two parameters are fed back to the first $L-1$ RD maps because the first iteration of integration with L frames as the input only outputs one set of results.

Similarly, the signal within the new RD map obtained with the frame whose index is $u \in \{L, L+1, \ldots, R\}$ can be expressed as

$$\mathrm{RD}_{u\_\mathrm{res}}(\tau, f_a) = A_{u\_\mathrm{res}} \rho\left(\tau - \frac{kR_{u\_\mathrm{res}}}{c}\right) \times \mathrm{sinc}\left[T\left(f_a - f_{u\_\mathrm{res}}\right)\right] * \exp\left(j\varphi_{u\_\mathrm{res}}\right) + N_{u\_\mathrm{res}}. \tag{32}$$

The positions of the target peaks, which are obtained from these SNR-enhanced signals described by (31) and (32), form the confirmed target track in the RD domain. Some discussions regarding the proposed C-DP-TBD algorithm are given as follows.

1) *The choice of frames to be integrated:* The minimum value of L can be calculated directly by (14), and two considerations arise in this context. First, for the C-DP-TBD algorithm, incorporating more frames for integration could potentially enhance the final SNR, but the algorithm is dependent on a prerequisite in practice. This prerequisite indicates that the power distribution of the target peak within the RD map should remain consistent or highly similar across these frames for coherent integration. Inconsistency of the power distribution not only may lead to the loss of the target's characteristic parameters, such as the number of target scatting points along the range direction, but also makes it difficult to determine whether the final peak accurately represents a target. Second, the relative motion of the target with respect to the receiver, such as turning, can induce a shift in the distribution of the target peak and then can deteriorate the performance of coherent integration. In this case, only adjacent frames are suitable for coherent integration, and it is advisable to keep L relatively small to mitigate the aforementioned power shift and reduce the time consumption.

2) *The false target peak after integration:* The occurrence of a false track arises when a persistently stable noise spike can be found in all RD maps, similar to the characteristics of a target. This hypothetical scenario becomes more plausible if the noise spike consistently exhibits a higher amplitude than that of the actual target returns. However, such instances are rarely observed in the case of random noise because the background noise is inherently stochastic in most instances.

3) *The refinement of search procedures:* Due to the lack of prior knowledge about the target, the initial detection should be conducted with a wide search range, covering all possible motion parameters, as indicated by (22). Fortunately, after extracting motion information of the target from the first L frames, both M and P can be significantly reduced based on the detection results obtained from the first L frames. At least, the orientation of motion can be determined. Therefore, M and P are not constant for each frame in the step of normal detection, depending on the previous detection results. In addition, concerning the phase search in each frame, a large value of σ can be initially set to identify the target's location and a coarse phase shift. Subsequently, the search can be refined with a finer value of σ at that specific location of the target in the RD domain to acquire the phase with higher accuracy.

4) *Detection of multiple targets:* The proposed algorithm is tailored to deal with the single-target detection problem. When multiple targets exist within the search range, the tracking process may fail. This is because the target with weaker echoes is removed in each iteration, and the amplitude difference among the peaks of these possible targets may not be constant. In practical operation, since the number of targets to be detected is unknown, it is essential to store all peaks with SNR surpassing the threshold γ_2 if the location of a peak in the RD domain differs from that of other candidate peaks. Each peak corresponds to a potential target. Moreover, it is a challenging task to design an algorithm to determine tracks for all of these targets. Therefore, this article does not involve the problem of multiple-target TBD.

5) *Target detection performance analysis:* To demonstrate the effectiveness of our proposed detector and its response to input signals with different values of SNR, a Monte Carlo simulation was conducted to produce the receiver operating characteristic (ROC) curves. We first generated a set of received signals with -53 dB SNR. Then, we obtained the second set of received signals by processing the first set of received signals using the MFD procedure, as shown in Fig. 3. Here, the value of L was set to 2. We also generated the third set of received signals with an SNR of -50 dB for comparison. Each set of received signals comprised 20 000 radar returns, and half of these radar returns with a target present. The obtained ROC curves are depicted in Fig. 6. It can be found that the curve produced by the received signals with -50 dB SNR is closer to the upper left part compared with that produced by the received signals with -53 dB SNR. This indicates that received signals with a higher SNR can lead to superior detection performance. Fig. 6 also shows that the curve obtained by the third set of received signals with -50 dB SNR is similar to that obtained by the second set of received signals that are generated by processing the first set of received signals with -53 dB SNR using our proposed MFD procedure. This is reasonable because the coherent integration of two frames can result in an increase in SNR by a factor of 3 dB, i.e., $(10 * \log_{10} 2)$ dB. Therefore, it can be found that our proposed algorithm can improve the target detection performance.

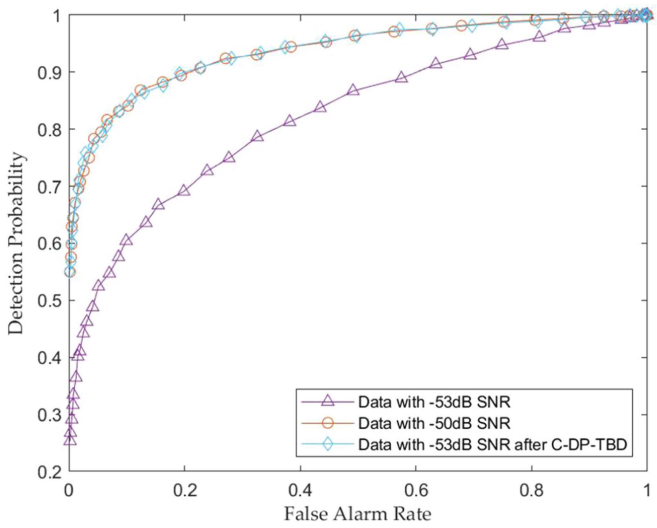

Fig. 6. ROC curves for our proposed detector.

IV. Simulation Results

In this section, simulation results are described in detail to demonstrate the weak target detection capabilities of the C-DP-TBD algorithm. The main simulation parameters are listed in Table I. Note that the initial target distance set in this simulation is not identical to the detection range of the algorithm because the energy loss of the signal during transmission is not considered in this simulation.

To clearly indicate the position of the target peak in the RD domain, raw simulation data were generated by introducing additive white Gaussian noise, resulting in an SNR of -45 dB.

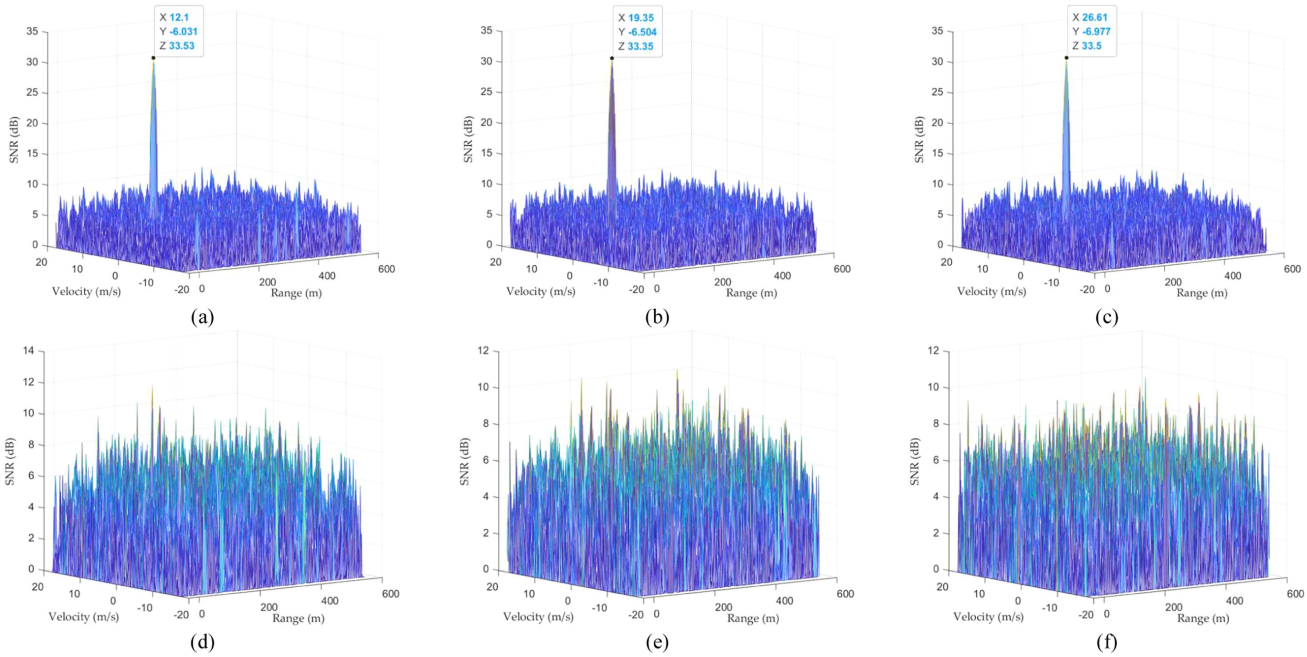

Fig. 7. Simulation results in the RD domain obtained with (a) third frame having an SNR of −45 dB, (b) fourth frame having an SNR of −45 dB, (c) fifth frame having an SNR of −45 dB, (d) third frame having an SNR of −67 dB, (e) fourth frame having an SNR of −67 dB, and (f) fifth frame having an SNR of −67 dB, respectively.

TABLE I
SIMULATION PARAMETERS

Item	Specification
Illuminator	BeiDou C01 B3I
Carrier frequency	1268.520 MHz
Chipping rate of ranging code	10.23 MHz
Period of ranging code	1 ms
Sampling rate	62 MHz
Pulse repetition frequency	1 kHz
Target's size	Point target
Target's reflection factor	1
Target's initial distance	0 m
Target's radial velocity	-5 m/s
Target's radial acceleration	-0.5 m/s^2
Total number of frames	10

Following range compression and the application of both KT and DA, the generated RD maps corresponding to the third to fifth frames are depicted in Fig. 7(a), (b), and (c), respectively. Subsequently, the target was left to be buried by noise with increased power to simulate the practical observation, resulting in a decrease in SNR to −67 dB. The RD maps generated with the new third to fifth frame data are presented in Fig. 7(d), (e), and (f), respectively. Each frame was generated with a CPI of 1 s, and the reason for this selection can be found in our previous work [26].

Before utilizing the weak target detection technique, we need to calculate $\mathrm{CPI}_{\min}$ and $\mathrm{CIL}_{\min}$. In this simulation, we set the threshold γ_2 to 15 dB and the value of max_miss to 3, respectively. If the RD map was generated with raw data with an SNR of −45 dB, an increase in the SNR of the target peak to around 33.5 dB can be obtained after RD processing, which is sufficiently high for target detection. However, for raw data whose SNR is −67 dB, the target was buried by background noise because a decrease in the SNR of the target peak to around 11.5 dB can be found even with effective DCM correction and was below the detection threshold. According to (13), $\mathrm{CPI}_{\min}$ was calculated to be 2.24 s in this case, and the minimum CIL should be 3 according to (14).

Since the actual motion parameters were manually set and fully known, the variables M and P were set to be 1 based on the given radial velocity and acceleration, leaving only the phase term as an unknown term. Therefore, the upper bound of CPI was calculated to be 3.11 s in terms of (15) along with the preset acceleration, as given in Table I. Therefore, we set CIL to 3 for MTD and a CPI of 3 s for single-frame MTD in this simulation to acquire the same integration time length for each algorithm.

Three distinct weak target detection strategies were applied to process these ten frames to detect the target from the noise with increased power. First of all, the traditional DP-TBD algorithm without interframe phase compensation was implemented to search the target peak's locations in the RD domain, and each frame was integrated noncoherently with the nearest frames. The results are illustrated in Fig. 8(a)–(c). Subsequently, the traditional MTD method was executed with a CPI of 3 s, while the RCM and DCM correction algorithms remained consistent with those outlined in Section III. The corresponding results are given in Fig. 8(d)–(f). Finally, the proposed C-DP-TBD algorithm was implemented, and the SNR-enhanced RD maps obtained with the three frames are presented in Fig. 8(g)–(i).

For the DP-TBD algorithm, Fig. 8(a)–(c) shows that the target peak can be identified in each RD map, but its SNR does not

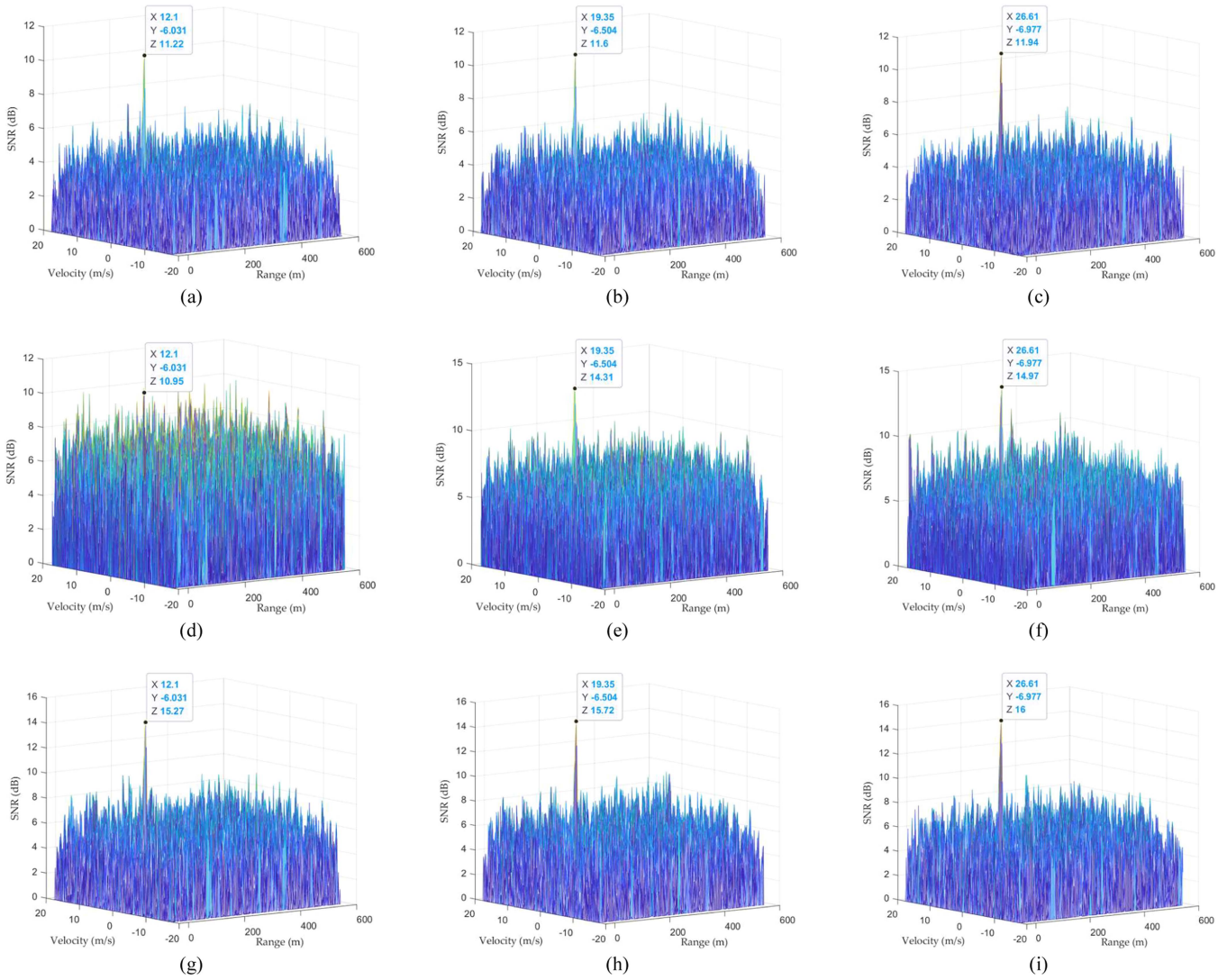

Fig. 8. RD maps obtained with (a) third frame processed by the DP-TBD algorithm, (b) fourth frame processed by the DP-TBD algorithm, (c) fifth frame processed by the DP-TBD algorithm, (d) third frame processed by the MTD algorithm with a CPI of 3 s, (e) fourth frame processed by the MTD algorithm with a CPI of 3 s, (f) fifth frame processed by the MTD algorithm with a CPI of 3 s, (g) third frame processed by the C-DP-TBD algorithm, (h) fourth frame processed by the C-DP-TBD algorithm, and (i) fifth frame processed by the C-DP-TBD algorithm, respectively.

reach the preset SNR threshold γ_2 in this simulation. Therefore, DP-TBD failed to detect the target due to the insufficient SNR. It is worth mentioning here that the SNR is defined as the ratio between the power of each data point and the average power of the noise background in our work. This definition is similar to the classical definition of SNR, and the only difference is that this ratio is calculated individually for each point within the RD map in our work. As described in Section III-A, the originally defined SNR cannot be used to demonstrate the performance of noncoherent integration for RD maps because the power increase rates of both signal and background noise are almost the same. To more accurately demonstrate the performance of noncoherent integration, a new method used to calculate SNR by incorporating the standard deviation of the disturbance background can be found in [17]. Nevertheless, we found that this alternative calculation of SNR cannot effectively demonstrate the distinctions between the two MFD methods employed in this simulation when CIL was set to 3. Therefore, we still adopted the traditional definition of SNR for the analysis of processed results.

For the single-frame MTD algorithm, its instability detection performance can be found for the three frames, as shown in Fig. 8(d)–(f), and the noise background appears to be more chaotic compared with the DP-TBD and C-DP-TBD algorithms. Traditional MTD methods heavily rely on the maintenance of intraframe coherence, which is mainly achieved by DCM correction. However, the performance of MTD methods is significantly influenced by the target scintillation. This is because it is challenging to search for a constant Doppler rate within one range bin and to compensate for the phase shift in the presence of target scintillation. Note that if a shorter CPI is adopted, the influence of target scintillation will be reduced significantly. To simulate the effect of target scintillation, DCM correction was implemented by phase compensation with a preset acceleration

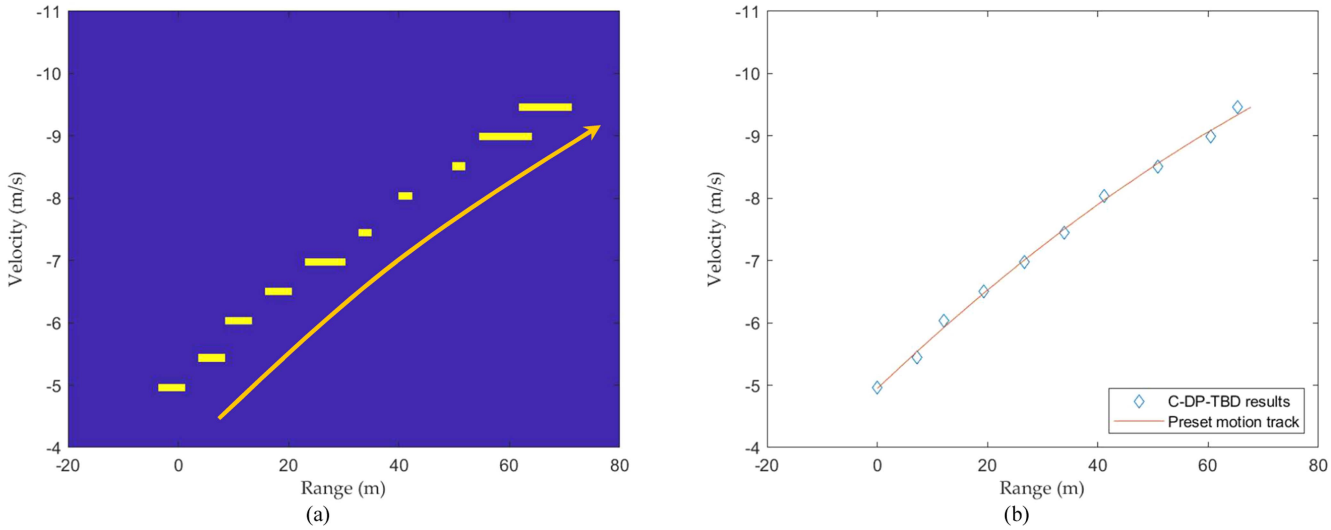

Fig. 9. (a) Detection results obtained by the C-DP-TBD algorithm after threshold segmentation and (b) comparison between the motion track of the target extracted from (a) and the preset target track. Here, the orange curved arrow represents the motion trend of the target.

in two MFD algorithms. In contrast, DA was employed to search for the Doppler rate in the single-frame MTD algorithm. This discrepancy accounts for the insufficient SNR in these RD maps obtained by the single-frame MTD algorithm, even though a CPI of 3 s should be adequate for this method to acquire an SNR that can surpass the threshold in theory. A more detailed discussion of the performance of the single-frame MTD algorithm will be provided in Section V.

Fig. 8(g)–(i) shows that an increase in signal amplitude by a factor of three can be obtained by the C-DP-TBD algorithm for each frame, resulting in an increase in SNR to approximately 15.5 dB because of an increase in the noise amplitude by a factor of $\sqrt{3}$. With this enhancement, the SNR of the target peak can surpass the preset threshold of 15 dB, making the target easily distinguished from the background noise. Therefore, for the three algorithms adopted in this simulation, Fig. 8 shows that C-DP-TBD is the only effective method for weak target detection.

After threshold segmentation, the detection results obtained by the C-DP-TBD algorithm are shown in Fig. 9(a), and a comparison between the motion track of the target extracted from Fig. 9(a) and the preset target track in the RD domain is illustrated in Fig. 9(b). The results, as shown in Fig. 9, demonstrate that the weak target in the case of -65 dB SNR can be successfully detected and tracked with the C-DP-TBD algorithm and are well consistent with the preset target motion track.

V. Experimental Results

The experiment was conducted on the Yangtze River Bridge in Wuhan, with the target being a ferry crossing the river. Our radar system, as shown in Fig. 10(a), included one left-handed circular polarization (LHCP) antenna connected to the radar channel and one right-handed circular polarization antenna connected to the heterodyne channel, as described in Section II. The photograph of the target is shown in Fig. 10(b) and the experimental scenario is depicted in Fig. 10(c). Here, the satellite image was captured from Google Earth. The sampling duration was 30 s, and the BDS GEO C02 satellite was employed as the illuminator. Fig. 10(d) shows the azimuth and elevation angles of the C02 satellite and the target at the beginning of sampling. Here, the receiver's position was set as the origin of the local coordinate system. For the bistatic configuration where the C02 satellite was adopted as the transmitter of opportunity, the coefficient k given by (1) can be set to 2, making the bistatic configuration simplified to be a quasi-monostatic configuration. Note that the other two satellites, i.e., medium Earth orbit C34 and GEO C60, have similar azimuth and elevation angles to the C02 satellite and can provide alternative bistatic configurations in which the value of coefficient k is close to 2. However, early stage data processing results indicated that, when the C02 satellite was used as the transmitter, the received echo signals had the lowest SNR among the three satellite candidates. Therefore, C02 was chosen for further analysis to demonstrate the effectiveness of the proposed algorithm.

Before presenting the processing results, we analyzed both the range and motion parameters of the target to predict the possible target track in the RD domain and to determine the limits of radial velocity and acceleration. According to AIS data, the radial distance of the target was around 300 m, and its absolute velocity was approximately 4 m/s. During the sampling period, the target was crossing the river, as well as the radial direction of our radar system. Since the radial velocity of a target can be obtained through the projection of the absolute velocity vector onto the radial direction, the absolute velocity can be regarded as the lower bound of the velocity, and its specific range can be initially set from -4 to 0 m/s. The negative sign comes from the fact that the ferry was driving away from the receiver during the observation period. Moreover, since the angle between the receiver-to-target direction and the radial direction increased slowly during the observation period, the preset acceleration

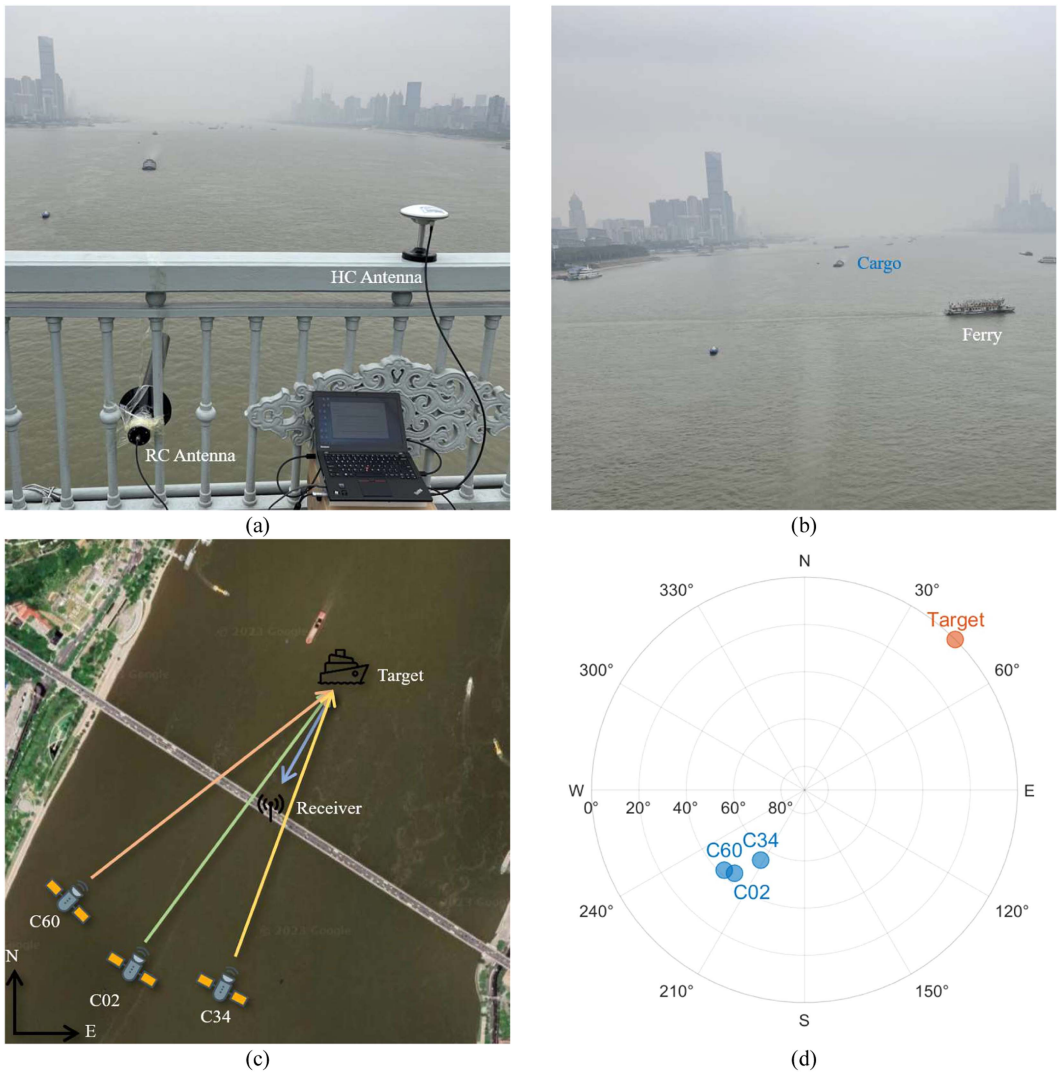

Fig. 10. (a) Experimental setup of our radar system, (b) photograph of the target, (c) schematic diagram of the acquisition geometry during the experiment, and (d) azimuth and elevation angles of BDS C02, C34, and C60 satellites and the target with respect to the receiver.

ranges from -0.5 to 0 m^2/s. Finally, due to the target scintillation among frames and the resolution of the RD map, i.e., the range resolution is about 2.4 m and the azimuth resolution is 0.12 m/s, the range of velocity was extended from -5 to 3 m/s, and the range of acceleration was extended from -0.5 to 0.25 m^2/s. Although the upper bounds of velocity and acceleration might exceed their corresponding theoretical values, the algorithm can have a greater tolerance for raw data errors generated in the sampling process and fluctuations produced in the intermediate frequency signal processing. In terms of the target motion track shown in the RD maps, we found that the target had already passed the radial direction of our radar at the beginning of the sampling process. Therefore, the entire target motion track in the RD domain should be located in the negative velocity plane, and its variation trend should be toward smaller velocity and larger radial range.

After RD map generation using the MTD algorithm with a CPI of 1 s for each frame, a total of 30 RD maps were obtained. The processed results of the 13th–15th frames without any integration technique are shown in Fig. 11(a)–(c), respectively. In our experiment, the threshold γ_2 was set to be 13 dB and the value of max_miss was set to 3. Fig. 11 clearly shows that no obvious peaks within these frames have SNR larger than the required level. In other words, a typical weak target detection problem needs to be solved. Note that the peak observed at the range of 0 m corresponds to the direct signal leaking into the LHCP antenna. It was not removed from the RD map and used as a reference position instead.

Since the target peak cannot be identified from the background noise, it is impossible to analyze the SNR with these original RD maps. Instead, the value of SNR_{input} was initially set to the power level of the prominent noise peak, indicating a scenario where the target peak is just buried by the background noise. If the input SNR after integration remains insufficient for target detection, it should be assigned a lower value for the next round of analyses. Based on the above analyses, SNR_{input} was set to

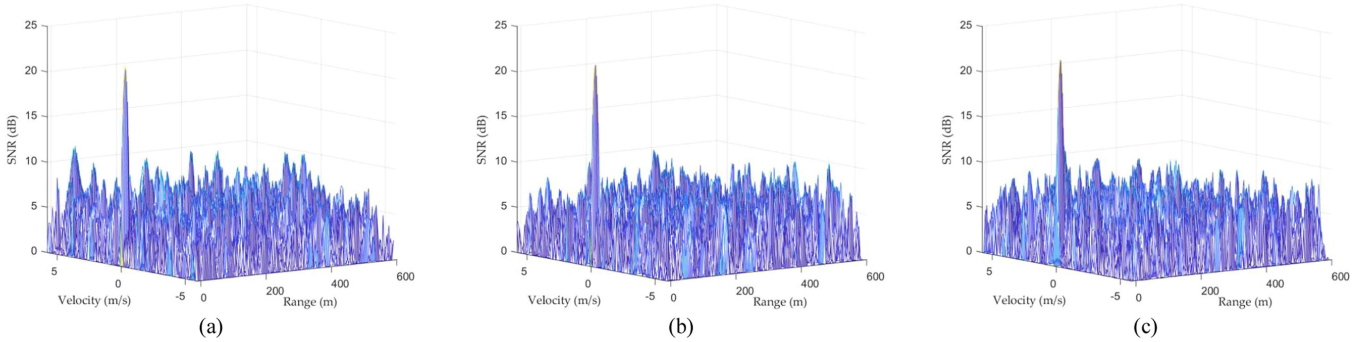

Fig. 11. Original RD maps obtained with (a) 13th frame, (b) 14th frame, and (c) 15th frame, respectively. Here, the BDS C02 satellite was used as the transmitter of opportunity.

9 dB in this experiment. Another approach to setting this value is to consider the peak SNR obtained from the noncoherently integrated RD maps. This is because noncoherent integration can enhance the distinguishability of the target, although the SNR of the target echo remains almost unchanged compared with the original RD map. Moreover, the value of $\mathrm{CPI}_{\min}$ was calculated to be 2.51 s in terms of (13), and hence, we set CIL to be 3. On the other hand, the value of $\mathrm{CPI}_{\max}$ was calculated to be 3.11 s according to (15), and therefore, we still chose a CPI of 3 s for MTD. Then, DP-TBD, traditional MTD, and C-DP-TBD algorithms were used to process the 13th–15th frames in turn. The corresponding processed results are shown in Fig. 12.

For the DP-TBD algorithm, Fig. 12(a)–(c) shows that a distinguishable target peak can be identified for these three frames, but its SNR is well below the preset threshold. For long-time integration or traditional MTD algorithms, as shown in Fig. 12(d)–(f), a distinguishable target peak can also be observed for all three frames. However, the location of the echo peak corresponds to a stationary target with a radial velocity of 0 m/s, which contradicts our prior information about the ferry's motion. As shown in Fig. 10(b), only a cargo marked with blue characters has a longer radial range than the ferry. However, according to AIS data, the cargo was traveling at a velocity of about 5 m/s during the observation period. After further examination, we found that these spikes shown in the RD maps were more likely produced by echo signals scattered by the river surface. This is because for each target's track generated by different satellites in the RD domain, a similar "stationary target" can always be found but with a different bistatic range according to the varied bistatic radar configuration. Compared with the DP-TBD algorithm, the MTD algorithm with a long CPI can be used to detect weak targets whose motion can be well compensated, such as the echo signals scattered by the river surface in this case. Note that this kind of target was not successfully detected by the DP-TBD algorithm with a shorter integration interval, as shown in Fig. 12(a)–(c). However, the detection of maneuvering weak targets, whose motion parameters are difficult to predict, was not achieved with the MTD algorithm in our experiment.

Through examining the RD maps obtained by C-DP-TBD, as shown in Fig. 12(g)–(i), it is evident that the weak target can be successfully detected with this algorithm, and these target peaks in RD maps exhibit adequate high SNR and can further provide the radial range and velocity information of the detected target. Furthermore, an increase in SNR by a factor of around 4.7 dB in each map obtained by C-DP-TBD can be observed compared with the case of DP-TBD. Regarding the locations of the target peak, as shown in Fig. 12(g)–(i), it can be observed that the target peak moved backward by one range cell in the 14th frame compared with the 13th frame. This is attributed to the target scintillation mentioned earlier and highlights the importance of extending the search range for motion parameters. Moreover, it can be observed that the bistatic range of the target remains almost constant for the three frames. This is attributed not only to target scintillation but also to the low radial velocity of the target as well as the low range resolution achieved by GNSS signals. In addition, similar to DP-TBD, the peak of the echo signal produced by the river surface reflection was not identified as a target in these RD maps obtained by C-DP-TBD. This is because the echo signal produced by the river surface reflection has a lower SNR than that produced by the ferry, and it is further submerged by background noise after the coherent integration with no interframe compensation for it. This reason also explains why the peak corresponding to the direct signal experiences an SNR reduction after the implementation of the C-DP-TBD algorithm. For the 15th frame, Fig. 12(i) shows that the RD map produced by the C-DP-TBD appears "messier" than that obtained by DP-TBD, which may seem counterintuitive. This is because coherent integration can smooth noise by leveraging the randomization of the noise's phase.

Now, let us present the target's RD history obtained by noncoherently integrating RD maps. The RD histories generated from original RD maps obtained by MTD with a CPI of 1 s and these RD maps obtained by DP-TBD, MTD with a CPI of 3 s, and C-DP-TBD are shown in Fig. 13(a), (b), (c), and (d), respectively. As shown in Fig. 13(b) and (d), the target's complete motion tracks in the RD domain generated from maps obtained by DP-TBD and C-DP-TBD can be clearly seen, and a higher SNR can be found in the latter subfigure. Although both tracks provide correct motion information of the detected target, a unified threshold γ_2 indicates that only the results obtained by C-DP-TBD are qualified. Fig. 13(a) shows a faint motion track of the target, even though the SNR is below the threshold. In

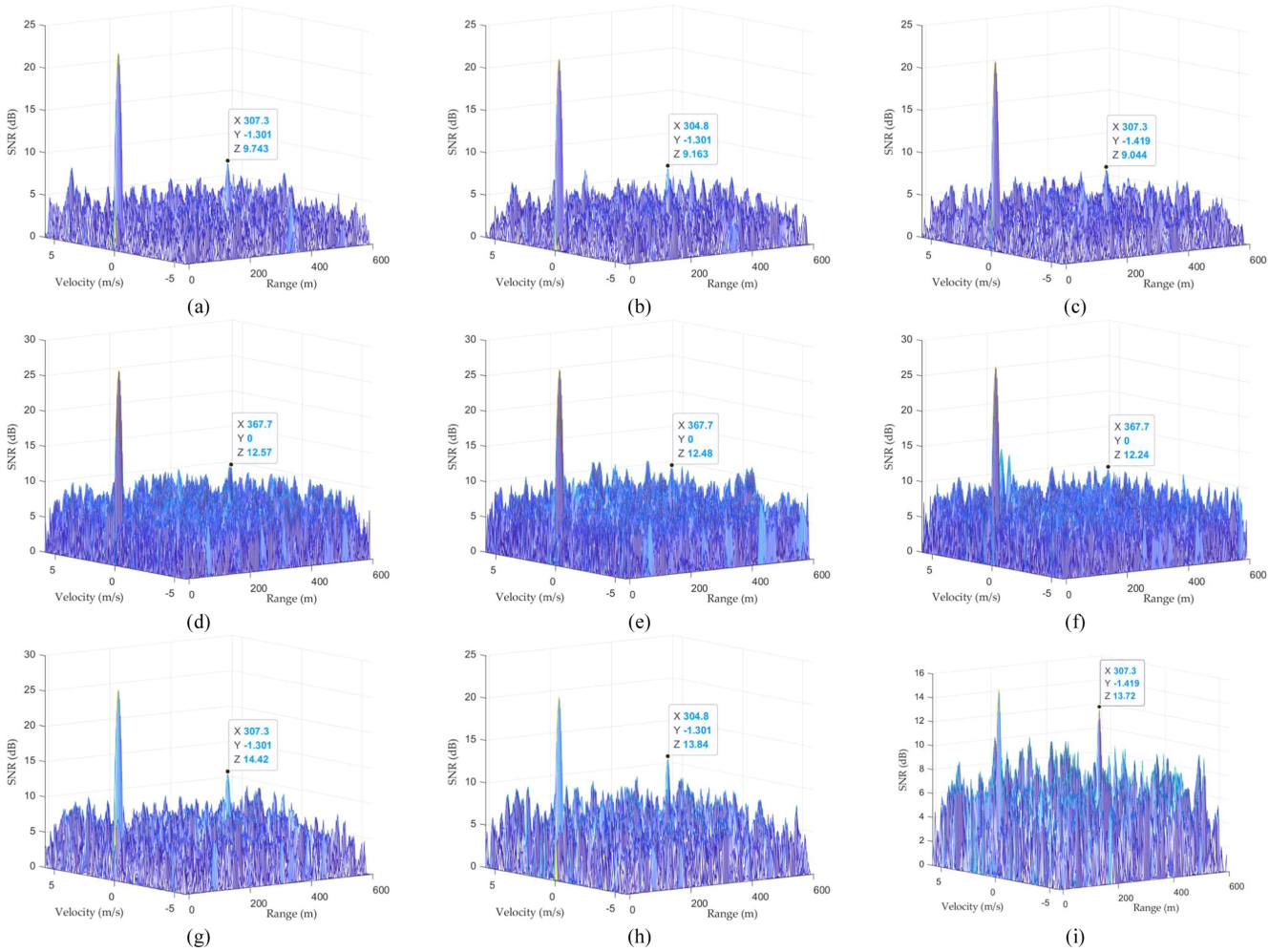

Fig. 12. RD maps generated from (a) 13th frame processed by the DP-TBD algorithm, (b) 14th frame processed by the DP-TBD algorithm, (c) 15th frame processed by the DP-TBD algorithm, (d) 13th frame processed by the MTD algorithm with a CPI of 3 s, (e) 14th frame processed by the MTD algorithm with a CPI of 3 s, (f) 15th frame processed by the MTD algorithm with a CPI of 3 s, (g) 13th frame processed by the C-DP-TBD algorithm, (h) 14th frame processed by the C-DP-TBD algorithm, and (i) 15th frame processed by the C-DP-TBD algorithm.

contrast, the target's motion track cannot be identified in the results obtained by MTD with a long CPI, mainly due to the failure of DCM correction.

Following the threshold segmentation applied for each frame, the results obtained by the C-DP-TBD algorithm are depicted in Fig. 14(a), and a comparison between the motion track of the target extracted from Fig. 14(a) and those provided by the AIS data is illustrated in Fig. 14(b). The results, as shown in Fig. 14, demonstrate that a clear and accurate motion track of the target can be acquired by the C-DP-TBD algorithm, which is characterized by sufficient high peak SNR and acceptable levels of track error.

Finally, the computational complexity is analyzed by computing the average processing time of all 27 frames on a computer with a processor of Intel Core i7-10875H. After the original RD maps have already been generated, the total computing time is 0.06 s for DP-TBD and 51.98 s for C-DP-TBD. These statistical results were obtained based on 160 possibilities for each iteration in DP-TBD, which are achieved by the reduction of the search range due to prior knowledge of this specific task. In addition, the value of Q given by (20) was set to 32, which is proven to be the optimal value to compromise the accuracy and computational complexity according to our test. It can be found that the time cost of the two algorithms differs by three orders of magnitude, mainly attributed to the square of Q. Therefore, the remarkable capability of weak target detection of the C-DP-TBD algorithm is achieved at the expense of increased computational complexity. Since both computational efficiency and target detection capability are significant performance parameters for a radar system, the choice between DP-TBD and C-DP-TBD methods should be made based on the specific requirements and constraints of the sounding application. It is worth mentioning here that the specific computational complexity highly depends on the search parameter settings and the performance of the signal processing hardware. In addition, for MTD with a long CPI, its statistical results of computational complexity were not collected for comparison. This is because MTD is only used for RD map generation, and hence, comparisons with the other two MFD methods, which take RD maps as input, are not appropriate.

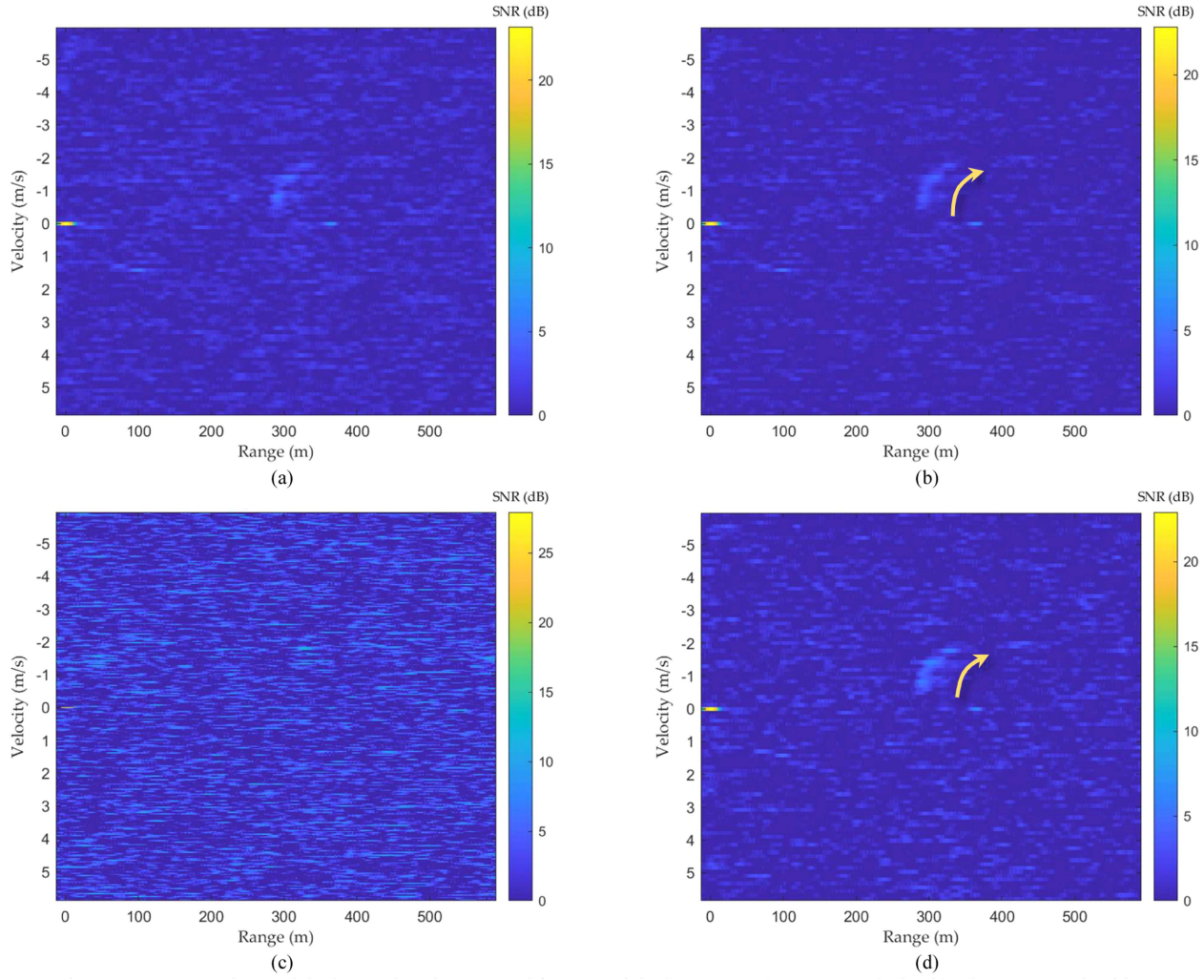

Fig. 13. Target's motion track in the RD domain generated from (a) original RD maps, (b) RD maps obtained by the DP-TBD algorithm, (c) RD maps obtained by the MTD algorithm with a CPI of 3 s, and (d) RD maps obtained by the C-DP-TBD algorithm. Here, the orange curved arrow denotes the changing trend of the target track.

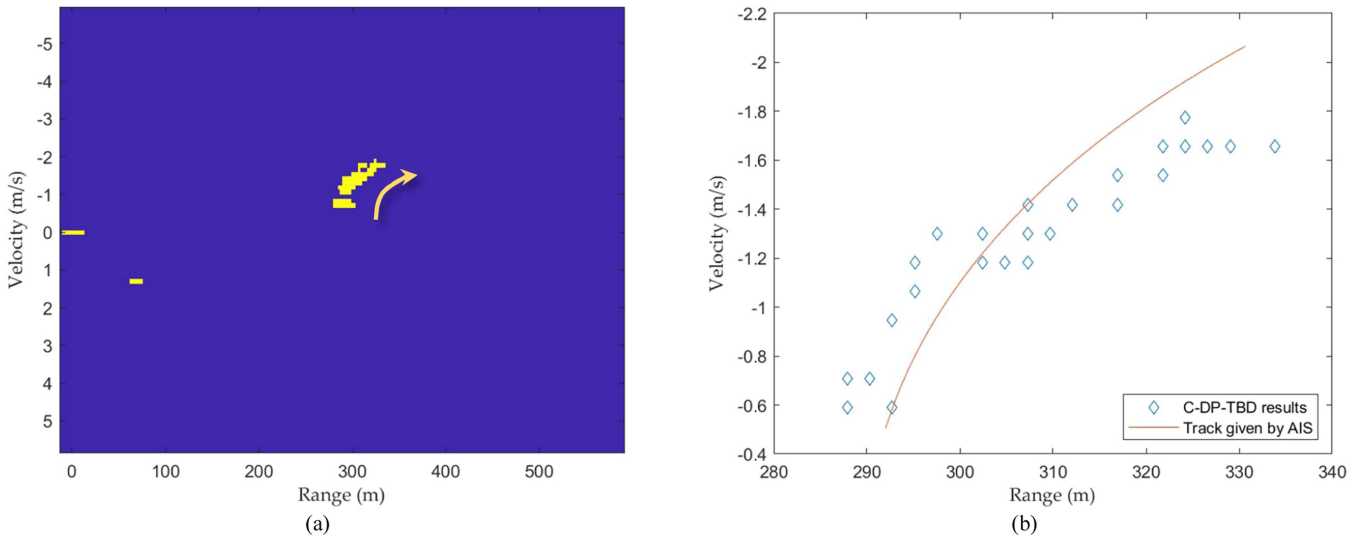

Fig. 14. Detection results obtained by the C-DP-TBD algorithm after threshold segmentation and (b) comparison between the motion track of the target extracted from (a) and those provided by the AIS data. Here, an orange curve represents the motion trend of the target.

VI. Conclusion

A novel algorithm referred to as C-DP-TBD has been presented for remote sensing of weak targets using GNSS bistatic radar of opportunity. In terms of these comparisons using simulation and experimental data, it can be found that the proposed algorithm has a better performance for weak target detection compared with the traditional MTD with long CPI and DP-TBD methods. However, the remarkable capability of weak target detection of the C-DP-TBD algorithm is achieved at the expense of increased computational complexity.

In future work, further improvements of the C-DP-TBD algorithm will be conducted from the following four aspects. First, the search process of interframe phase shift will be improved to reduce the computational complexity. Second, the C-DP-TBD algorithm, in which multiple GNSS satellites are used as transmitters of opportunity simultaneously, will be proposed to achieve better weak target detection performance. Undoubtedly, this task will introduce a more challenging scenario than that presented in this article due to the varying power distribution of target peak in the case of different transmitters, as well as the increased unpredictability of interframe phase shifts among echo data acquired from different satellites. Third, the C-DP-TBD algorithm presented in this article is tailored to deal with the single-target detection problem because the discrepancy in interframe phase shifts for different targets may potentially lead to tracking failure. Consequently, the C-DP-TBD algorithm will be improved to detect multiple moving targets. Finally, the performance of the C-DP-TBD algorithm has been validated using a stationary ground-based receiver in this study, and we will continue to validate its performance with airborne or spaceborne receivers.

References

[1] C. D. Hall and R. A. Cordey, "Multistatic scatterometry," in *Proc. Int. Geosci. Remote Sens. Symp., 'Remote Sens., Moving Toward 21st Century'*, 1988, pp. 561–562, doi: 10.1109/IGARSS.1988.570200.

[2] N. Rodriguez-Alvarez and J. L. Garrison, "Generalized linear observables for ocean wind retrieval from calibrated GNSS-R delay–Doppler maps," *IEEE Trans. Geosci. Remote Sens.*, vol. 54, no. 2, pp. 1142–1155, Feb. 2016, doi: 10.1109/TGRS.2015.2475317.

[3] R. Balasubramaniam and C. S. Ruf, "Development and application of a GNSS-R error model for hurricane winds," *IEEE J. Sel. Topics Appl. Earth Observ. Remote Sens.*, vol. 17, pp. 2336–2346, Dec. 2023, doi: 10.1109/JSTARS.2023.3344371.

[4] A. Alonso-Arroyo, A. Camps, H. Park, D. Pascual, R. Onrubia, and F. Martin, "Retrieval of significant wave height and mean sea surface level using the GNSS-R interference pattern technique: Results from a three-month field campaign," *IEEE Trans. Geosci. Remote Sens.*, vol. 53, no. 6, pp. 3198–3209, Jun. 2015, doi: 10.1109/TGRS.2014.2371540.

[5] Z. Li, C. Zuffada, S. T. Lowe, T. Lee, and V. Zlotnicki, "Analysis of GNSS-R altimetry for mapping ocean mesoscale sea surface heights using high-resolution model simulations," *IEEE J. Sel. Topics Appl. Earth Observ. Remote Sens.*, vol. 9, no. 10, pp. 4631–4642, Oct. 2016, doi: 10.1109/JSTARS.2016.2581699.

[6] V. U. Zavorotny, S. Gleason, E. Cardellach, and A. Camps, "Tutorial on remote sensing using GNSS bistatic radar of opportunity," *IEEE Geosci. Remote Sens. Mag.*, vol. 2, no. 4, pp. 8–45, Dec. 2014, doi: 10.1109/TGRS.2014.2374220.

[7] M. Zribi et al., "Airborne GNSS-R polarimetric multiincidence data analysis for surface soil moisture estimation over an agricultural site," *IEEE J. Sel. Topics Appl. Earth Observ. Remote Sens.*, vol. 15, pp. 8432–8441, Sep. 2022, doi: 10.1109/JSTARS.2022.3208838.

[8] M. Antoniou and M. Cherniakov, "GNSS-based bistatic SAR: A signal processing view," *EURASIP J. Adv. Signal Process.*, vol. 2013, no. 1, Dec. 2013, Art. no. 98, doi: 10.1186/1687-6180-2013-98.

[9] W. An, M. Lin, and H. Yang, "Stationary marine target detection with time-series SAR imagery," *IEEE J. Sel. Topics Appl. Earth Observ. Remote Sens.*, vol. 14, pp. 6406–6413, Jun. 2021, doi: 10.1109/JSTARS.2021.3088845.

[10] G. Xiong, F. Wang, W. Yu, and T.-K. Truong, "Spatial singularity-exponent-domain multiresolution imaging-based SAR ship target detection method," *IEEE Trans. Geosci. Remote Sens.*, vol. 60, Sep. 2021, Art. no. 5215212, doi: 10.1109/TGRS.2021.3113919.

[11] W. Ji, C. Xiu, W. Li, and L. Wang, "Ocean surface target detection and positioning using the spaceborne GNSS-R delay-Doppler maps," in *Proc. IEEE Geosci. Remote Sens. Symp.*, 2014, pp. 3806–3809, doi: 10.1109/IGARSS.2014.6947313.

[12] A. Di Simone, H. Park, D. Riccio, and A. Camps, "Sea target detection using spaceborne GNSS-R delay-Doppler maps: Theory and experimental proof of concept using TDS-1 data," *IEEE J. Sel. Topics Appl. Earth Observ. Remote Sens.*, vol. 10, no. 9, pp. 4237–4255, Sep. 2017, doi: 10.1109/JSTARS.2017.2705350.

[13] T. Beltramonte et al., "Simulation-based feasibility analysis of ship detection using GNSS-R delay-Doppler maps," *IEEE J. Sel. Topics Appl. Earth Observ. Remote Sens.*, vol. 13, pp. 1385–1399, Mar. 2020, doi: 10.1109/JSTARS.2020.2970221.

[14] Y. Li, S. Yan, and J. Gong, "Target detection and location by fusing delay-Doppler maps," *IEEE Trans. Geosci. Remote Sens.*, vol. 61, Dec. 2022, Art. no. 5800114, doi: 10.1109/TGRS.2022.3232164.

[15] H. Ma et al., "Maritime moving target indication using passive GNSS-based bistatic radar," *IEEE Trans. Aerosp. Electron. Syst.*, vol. 54, no. 1, pp. 115–130, Feb. 2018, doi: 10.1109/TAES.2017.2739900.

[16] H. Ma, M. Antoniou, A. G. Stove, J. Winkel, and M. Cherniakov, "Maritime moving target localization using passive GNSS-based multistatic radar," *IEEE Trans. Geosci. Remote Sens.*, vol. 56, no. 8, pp. 4808–4819, Aug. 2018, doi: 10.1109/TGRS.2018.2838682.

[17] D. Pastina et al., "Maritime moving target long time integration for GNSS-based passive bistatic radar," *IEEE Trans. Aerosp. Electron. Syst.*, vol. 54, no. 6, pp. 3060–3083, Dec. 2018, doi: 10.1109/TAES.2018.2840298.

[18] Y. Barniv, "Dynamic programming solution for detecting dim moving targets," *IEEE Trans. Aerosp. Electron. Syst.*, vol. AES-21, no. 1, pp. 144–156, Jan. 1985, doi: 10.1109/TAES.1985.310548.

[19] E. Grossi, M. Lops, S. Member, and L. Venturino, "A novel dynamic programming algorithm for track-before-detect in radar systems," *IEEE Trans. Signal Process.*, vol. 61, no. 10, pp. 2608–2619, May 2013, doi: 10.1109/TSP.2013.2251338.

[20] S. Qin, J. Ding, L. Wen, and M. Jiang, "Joint track-before-detect algorithm for high-maneuvering target indication in video SAR," *IEEE J. Sel. Topics Appl. Earth Observ. Remote Sens.*, vol. 14, pp. 8236–8248, Aug. 2021, doi: 10.1109/JSTARS.2021.3104603.

[21] F. Santi and D. Pastina, "Application of track-before-detect techniques in GNSS-based passive radar for maritime surveillance," in *Proc. IEEE Radar Conf.*, 2019, pp. 1–6, doi: 10.1109/RADAR.2019.8835540.

[22] F. Santi, D. Pastina, and M. Bucciarelli, "Experimental demonstration of ship target detection in GNSS-based passive radar combining target motion compensation and track-before-detect strategies," *Sensors*, vol. 20, no. 3, 2020, doi: 10.3390/s20030599, Art. no. 599.

[23] W. Kun and Z. Xiaoling, "A TBD method using multi-frame coherent integration," in *Proc. 3rd Int. Asia-Pacific Conf. Synthetic Aperture Radar*, 2011, pp. 1–4.

[24] X. Li, Y. Yang, Z. Sun, G. Cui, and T. S. Yeo, "Multi-frame integration method for radar detection of weak moving target," *IEEE Trans. Veh. Technol.*, vol. 70, no. 4, pp. 3609–3624, Apr. 2021, doi: 10.1109/TVT.2021.3066516.

[25] M. Wang, X. Li, Z. Zhang, G. Cui, and T. S. Yeo, "Coherent integration and parameter estimation for high-speed target detection with bistatic MIMO radar," *IEEE Trans. Geosci. Remote Sens.*, vol. 61, Jul. 2023, Art. no. 5107915, doi: 10.1109/TGRS.2023.3298825.

[26] C. Zhang, S. Shi, S. Yan, and J. Gong, "Moving target detection and parameter estimation using BeiDou GEO satellites-based passive radar with short-time integration," *IEEE J. Sel. Topics Appl. Earth Observ. Remote Sens.*, vol. 16, pp. 3959–3972, Apr. 2023, doi: 10.1109/JSTARS.2023.3266875.

[27] W. J. Alberhseim, "A closed-form approximation to Robertson's detection characteristics," *Proc. IEEE*, vol. 69, no. 7, Jul. 1981, Art. no. 839, doi: 10.1109/PROC.1981.12082.

[28] D. Tufts and A. Cann, "On Albersheim's detection equation," *IEEE Trans. Aerosp. Electron. Syst.*, vol. AES-19, no. 4, pp. 643–646, Jul. 1983, doi: 10.1109/TAES.1983.309356.
[29] X. Zhou, P. Wang, H. Zeng, and J. Chen, "Moving target detection using GNSS-based passive bistatic radar," *IEEE Trans. Geosci. Remote Sens.*, vol. 60, May 2022, Art. no. 5113415, doi: 10.1109/TGRS.2022.3172217.
[30] W. Li, W. Yi, and K. C. Teh, "Greedy integration based multi-frame detection algorithm in radar systems," *IEEE Trans. Veh. Technol.*, vol. 72, no. 5, pp. 5877–5891, May 2023, doi: 10.1109/TVT.2022.3232785.

Ce Zhang received the B.S. degree in electrical engineering and automation from the Harbin Institute of Technology, Harbin, China, in 2016, and the M.S. degree in electrical and computer engineering from Rutgers University, Piscataway, NJ, USA, in 2018. He is currently working toward the Ph.D. degree in photogrammetry and remote sensing with the School of Remote Sensing and Information Engineering, Wuhan University, Wuhan, China.

His research interests include passive radar using global navigation satellite system satellites as transmitters and radar signal processing.

Shuzhu Shi received the B.S. degree in electric power automation from Xihua University, Chengdu, China, in 2004, and the Ph.D. degree in space physics from Wuhan University, Wuhan, China, in 2009.

From 2009 to 2011, he was an Engineer with the Nanjing Research Institute of Electronics Technology. From 2012 to 2015, he was a Postdoctoral Research Fellow with Global Navigation Satellite Systems Research Center, Wuhan University. From 2015 to 2018, he was a Lecturer with the School of Remote Sensing and Information Engineering, Wuhan University. From 2017 to 2018, he was a Visiting Scholar with Microwave Integrated System Laboratory, School of Engineering, University of Birmingham, Birmingham, U.K. Since 2018, he has been an Assistant Professor with the School of Remote Sensing and Information Engineering, Wuhan University. His research interests include passive radar using global navigation satellite system satellites as transmitters, remote sensing of electric power facilities using spaceborne or airborne synthetic aperture radar, ionospheric sensing, and high-frequency radar technology.

Jianya Gong received the Ph.D. degree in photogrammetry and remote sensing from the Wuhan Technical University of Surveying and Mapping, Wuhan, China, in 1992.

He is currently a Professor with the School of Remote Sensing and Information Engineering, Wuhan University, Wuhan, China. He is an Academician with the Chinese Academy of Sciences, Beijing, China. His research interests include remote sensing image processing, spatial data infrastructure, and geospatial data sharing and interoperability.

Dr. Gong is the President of the Commission VI of the International Society for Photogrammetry and Remote Sensing.

Rui Li received the B.S. degree in electronic information science and technology from Tiangong University, Tianjin, China, in 2017.

She is currently an Assistant Engineer with the Fourth Center of Beijing Institute of Remote Sensing Information, Beijing, China. Her research interests include space-based passive remote sensing systems and electromagnetic environment situational awareness.